Particle accumulation model in 3D reconstructed wall of a catalytic filter validated with time-resolved X-ray tomography

Marie Plachá[a], Martin Isoz[a,b], Petr Kočí[a,c,*], Matthew Jones[d], Miloš Svoboda[c], David Eastwood[d], Andrew York[e]

[a] *University of Chemistry and Technology, Prague, Technická 5, Prague 166 28, Czech Republic*
[b] *Institute of Thermomechanics, Czech Academy of Sciences, Dolejškova 5, Prague 182 00, Czech Republic*
[c] *New Technologies Research Centre, University of West Bohemia, Univerzitní 8, Pilsen 306 14, Czech Republic*
[d] *University of Manchester at Harwell, Diamond Light Source, Harwell Science & Innovation Campus, Didcot, Oxfordshire OX11 0DE, United Kingdom*
[e] *Johnson Matthey Technology Centre, Blounts Court Road, Sonning Common, Reading RG4 9NH, United Kingdom*

Abstract

A transient pore-scale model of particle deposit formation in 3D microstructure of a catalytic filter wall is introduced. It predicts location of particle deposits, dynamics of their growth, transition from deep to cake filtration regime as well as the impact on flow field, pressure drop and filtration efficiency. The model is validated against time-resolved X-ray tomography (XRT) data acquired during a filtration experiment. The validated model is then used in transient simulations of the soot filtration process in several different microstructures using cordierite filter substrate with varied Pd/alu catalyst distribution. The sample with the coating solely inside the wall pores provides the lowest initial pressure drop but suffers from low clean filtration efficiency and high pressure drop after the cake is formed. The sample with partial on-wall coating achieves not only a higher filtration efficiency but also a lower pressure drop in long-term operation.

Keywords: mathematical modeling, CFD, DPF, GPF, automotive exhaust

*Corresponding author.
Email address: petr.koci@vscht.cz (Petr Kočí)
URL: http://monolith.vscht.cz (Petr Kočí)

1. Introduction

One of the main pollutants present in exhaust gas from combustion engines burning carbonaceous fuels is the particulate matter (PM). Especially the fine particulate matter, comprising particles of diameter under 2.5 μm, has a widely reported negative influence on human health [1]. All over the world, the PM pollution is controlled via various emission limits. In Europe, the particulate matter has been restricted not only by its mass but also a number of particles since the norm Euro 6c (2017) for both diesel and gasoline engines. The latest legislation, Euro 6d (2020), requires the particle number emissions under 9.0×10^{11}#/km with the conformity factor of 1.5 during the real drive emissions (RDE) test, including the cold start phase [2]. For Euro 7, it is expected that the range of counted particles will be extended down to 10 nm (the current size limit is 23 nm and the smaller particles are excluded from the emission tests).

In order to meet the legal requirements on PM emissions, automotive exhaust gas aftertreatment systems are commonly equipped with particulate filters (PF), referred also as diesel particulate filters (DPF) and gasoline particulate filters (GPF) according to their application [2, 3, 4, 5]. Furthermore, PF can be combined with catalysts for conversion of gaseous pollutants to create a catalytic filter. The catalytic filter is a monolithic reactor comprising parallel channels that are alternately plugged at one end. Such a design forces the exhaust gas to flow through the channels walls that are porous and provide (i) filtration of particles (soot and ash), and (ii) conversion of gaseous pollutants in contact with the catalytic material.

A filter coated with three-way catalyst is beneficial in the exhaust gas aftertreatment systems for gasoline engines [6, 7, 8]. The filters in diesel engine vehicles is often combined with diesel oxidation catalyst [9, 10] or with a catalyst for selective catalytic reduction of nitrogen oxides [11, 12]. All these devices need to meet requirements that are typically anti-correlated: low pressure drop ver-

sus high catalytic conversion and filtration efficiency. These key performance parameters are strongly influenced by the device geometry, micro-structural morphology and PM loading [13].

The device geometry and micro-structural morphology is controlled during the filter production in order to optimize its performance. Previous studies included experimental work [14, 15, 16] and numerical models based on computational fluid dynamics (CFD) to identify suitable coating structure and location inside or on the filter walls and its impact on transport-limited conversion of gaseous pollutants [17, 18, 19], clean filtration efficiency [20] and pressure drop [21]. In parallel, models based on lattice Boltzmann method (LBM) were developed for the computation of clean filtration efficiency Belot et al. [22] and [23]. All the mentioned studies worked with 3D reconstructed section of porous wall with realistic catalyst distribution obtained from X-ray tomography (XRT) scans, however, they considered just a clean particulate filter.

Such a state corresponds only to a fraction of the filter life span due to the strong influence of soot accumulation on its performance. The soot/ash cake buildup improves the filtration performance, but it also increases its pressure drop and, consequently, the engine fuel consumption [24]. To identify the most suitable life-span morphology of a catalytic filter wall, a micro-structural model taking into account the growth of particle deposits inside the filter is required. Several models incorporating the soot deposition influence on the filter performance were recently developed. Li et al. [25] introduced an LBM model incorporating the soot accumulation. However, their model treats the soot deposits as an impermeable wall, similar to filter wall, which results in a nonphysically high pressure drop and limited percolation. Recently, more realistic LBM model including the soot cake permeability was developed Yamamoto and Yagasaki [26], enabling a parametric study of particle size influence on the filtration process. However, that model was limited to a bare filter without any catalytic coating.

In this paper, we present a transient model of particle deposit formation in 3D microstructure of a catalytic filter wall, including the impact of coated cat-

alytic material. In contrast to the LBM-based models [22, 25, 26], the presented filtration model is built on a weak coupling between an Eulerian CFD solver used to compute the flow field inside the filter wall and a Lagrangian tracking of soot particles. The soot deposits are transformed into porous zones in the CFD model and their volume is periodically updated on the basis of Lagrangian solver results. In turn, the deposited soot affects gas velocity and pressure field in the filter wall.

The newly proposed model is first validated against the data obtained by time-resolved, in-situ XRT of aerosol filtration [27] and then used for transient simulations of the soot filtration process in several different microstructures using cordierite filter substrate with various Pd/alu catalyst distributions. Attention is paid to the prediction of particle deposits location, dynamics of their growth, transition from deep to cake filtration regime as well as the impact on flow field, pressure drop and filtration efficiency, all depending on the distribution of catalyst in the filter microstructure. The ultimate goal is to identify suitable coating locations with respect to long-term operation including the impact of accumulated particles.

2. Experimental

The 3D microstructures used as simulation domains were obtained from the processed XRT images. First, a bare cordierite filter marked as BF0 was examined by time-resolved in-situ XRT during a filtration experiment at the I13-2 Diamond Manchester Imaging branchline at Diamond Light Source. The experimental setup is depicted in Figure 1. The cordierite filter had 300 cpsi, total length 29 mm, channel plug length 1 mm, wall thickness 216 μm, and wall porosity 63 %. During the filtration experiment, the gas inlet was allowed just to a single central channel. Using the volumetric flow rate of 21 ml/min, the mean superficial gas velocity through the wall was 0.0026 $\mathrm{m\,s^{-1}}$.

A direct experimental imaging of soot deposition in-situ is unfeasible due to its low density. Therefore, TiO_2 or ZnO nanoparticles have been proposed as

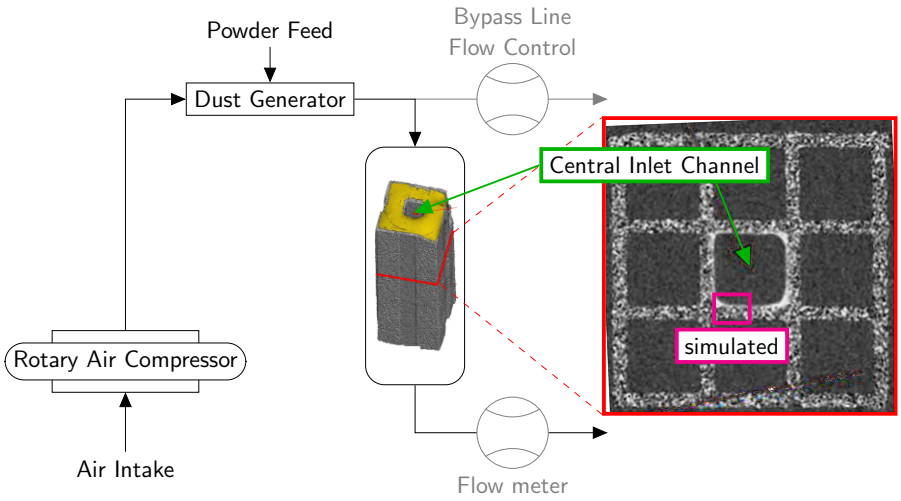

Figure 1: Simplified scheme of the experimental set-up.

suitable alternatives that provide sufficient contrast and allow reliable segmentation of the particle deposits inside the porous filter wall [27]. In this experiment, ZnO powder was used as particulate matter and the results were then utilized for validation of the newly developed transient filtration model. Figure 2 shows the measured particle size distribution in the ZnO aerosol. At the start-up, the inlet concentration of particles temporarily increased and only then reached a stable level. This might be due to dust generator start-up or re-entrainment of previously deposited particles in the lines. The temporary higher inlet concentration at the start-up was accounted for in the simulation, similarly as the actual density of ZnO particles that differs from soot, Sections 3.2–3.3.

The time-resolved XRT consisted of acquiring tomograms of the region of interest within the filter sample, then flowing aerosolized ZnO powder through the sample, redirecting the aerosol flow to bypass, and then re-imaging the region of interest. This was repeated to create a time series data set with images acquired after 0 s, 10 s, 30 s, 50 s and 110 s of cumulative aerosol loading.

For these tomograms a radiographic projection was acquired every 0.1° in an 180° fly scan (1800 projections) with exposure times of 0.03 s. Flat and dark field images were obtained at each time step in the experiment. The 'pink beam'

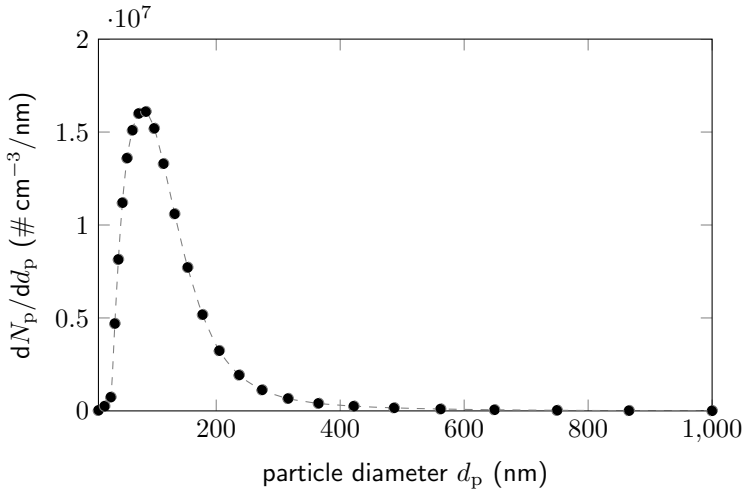

Figure 2: Particle size distribution of aerosolized ZnO powder measured in the experiment and used in the model validation simulations. Total steady concentration of particles was N_{p} =1.9×10^9 # cm^{-3}, increased five times during the start-up.

configuration at I13-2 with several harmonic peaks was used. The ID gap was set at 5 mm, and the Pt mirror was used; this already filtered the beam sufficiently so no extra filter was installed. Thus, the spectrum reaching the sample ranged from 6 to 29 keV, the peak flux was at 17 keV. The 2× objective was used for this workflow coupled to a LuAg scintillator. This 2× lens resulted in a total 4× magnification with pixel size of 1.625 μm. At the start of the beamtime the spectrum was optimised such that sufficient brightness and contrast between the deposit phase and background was observed in the radiographs.

Image processing and segmentation steps allowed the dataset to be segmented into pore/background, cordierite filter, and ZnO deposit phases for later quantification. Projections were reconstructed using the Filtered Back Projection algorithm from Astra in Savu [28] with ring removal, distortion correction, and dark-flat field correction [29, 30]. Each 3D image in the time series was then rotated, translated and cropped to the region of interest, a 553×1380×2440 μm^3 section. A histogram matching algorithm was then applied across the whole time series dataset.

Each of these 3D images in the time series was then registered onto the 'zeroth' image so that features were aligned across the times series. The 'zeroth' image is that which has no ZnO loading within it. The registration used methods from the Python distribution of SimpleITK. At this point the dataset was ready for segmentation. First a mask of the cordierite filter in the zeroth image was obtained using a simple intensity threshold. This was then applied to the ZnO loaded images to 'mask out' the cordierite phase such that the remaining high intensity pixels in the image belonged to the ZnO deposit, allowing for segmentation of the ZnO phase. By then combining the cordierite mask and ZnO mask from each time step we achieved full segmentation of the dataset.

In addition to the time-resolved XRT, a series of bare and coated catalytic filters was scanned by standard XRT at New Technologies Research Centre in Pilsen to obtain the information about the wall microstructure and coating location. These samples were prepared by vaccuum washcoating of Pd/γ-Al_2O_3 catalyst suspensions [15] on a cordierite filter substrate with 300 cpsi, wall thickness 216 μm and porosity of 66 %. The bare substrate sample from this series is denoted as BF1, and the related coated catalytic filters are denoted as CF1, CF2, and CF3. These catalytic filter samples use the same catalyst loading and differ only by the coating location: in-wall, combined on-wall and in-wall, and prevailing on-wall for CF1, CF2 and CF3, respectively.

The samples were scanned by X-ray tomograph Xradia MicroXCT 400 with source voltage 60 kV and power 6 W. The medium-size detector and 10$\times$ optical magnification results in resolution 2016$\times$2016 pixels and voxel size 1.113 μm. These XRT scans were segmented by brightness thresholds using the software package Fiji/ImageJ [31, 32] to identify substrate, coating and pore morphology [14, 17]. The structures BF1, CF1, CF2 and CF3 were then utilized in a simulation parametric study revealing the coating location influence on the transient soot filtration process.

Based on the processed and segmented XRT images, computational mesh for simulations was generated in OpenFOAM [33]. An illustrative reconstruction procedure of coated filter sample CF2 can be seen in Figure 3. A cut out

of the XRT data (Figure 3a) was transformed into a surface representation of present solid faces as depicted in Figure 3b. These were used for mesh generation by snappyHexMesh tool distributed with OpenFOAM, Figure 3c. In case of catalytic filters, the mesh includes also the coated catalyst zones so that gas transport through the coating is enabled in general. The meshes are unstructured with local refinement in the vicinity of the solid walls and at the coating boundary. The used computational domains ideally cover complete thickness of the filter wall and approximately one half of the channel width with final dimensions around $630\times320\times223$ μm^3. Each mesh consists of approximately 60 million cells.

3. Mathematical model

The reconstructed filter structures were employed in a computational framework represented by Figure 4. The proposed framework includes several interconnected solvers: flow, diffusion and reaction [17], solid particle movement [20], and the newly developed model for particles accumulation, growth of the filtration deposits and cake formation. In this paper we focus solely on the particles movement and accumulation in the wall microstructure during the filtration process.

Based on the results from [34], similarities between gasoline and diesel engines, and classification of coupling schemes and interactions between particles and flow introduced in [35], only one way coupling between the particles and the flow is assumed. Similarly, because the soot is diluted in the system with volumetric fraction below 0.1 ppm [34] and comprises small particles of $d_\mathrm{p} \lesssim 160\,\mathrm{nm}$ [20], instantaneous effects of the deposition on the flow are neglected and the system is simulated as decoupled, i.e., the flow is assumed at steady state during the simulation of solid particles movement and recalculated only after a deposition of significant volume as will be discussed in more detail in Section 3.3.

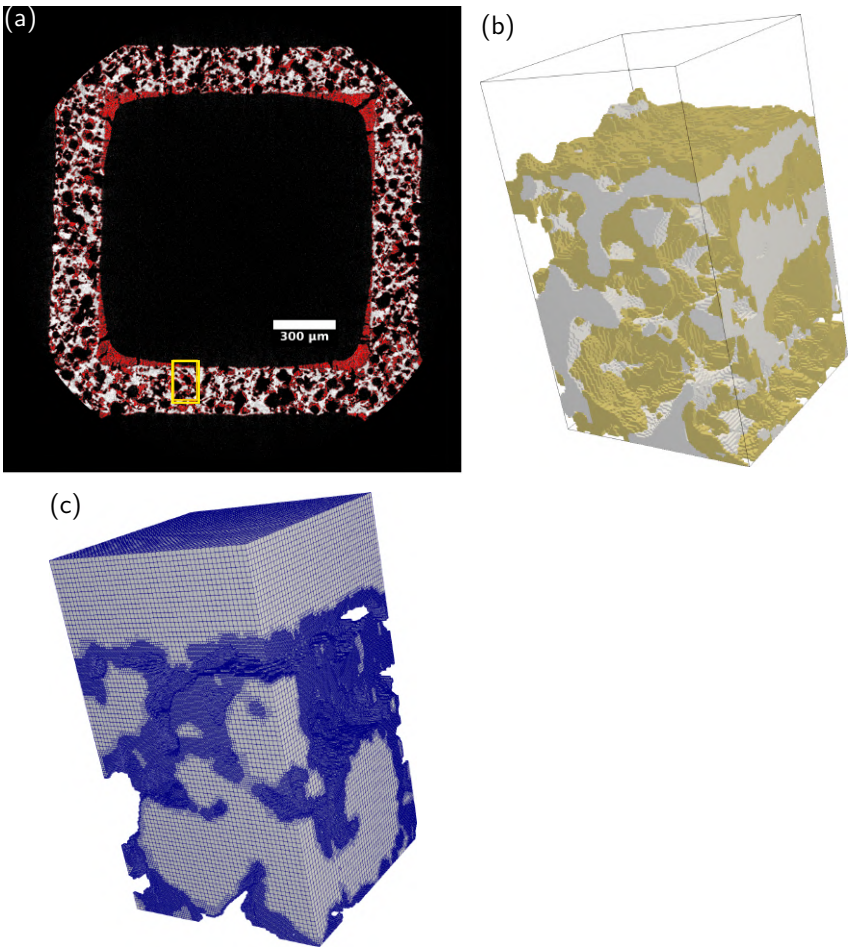

Figure 3: A reconstruction procedure of coated filter sample CF2 demonstrated on a small section of the wall (111×187×111 μm^3) a) one slice from 3D scan of the filter channel with the segmented substrate (white), catalytic coating (red), and free pores (black); b) surface representation of the wall subsection with substrate in grey and coating in yellow; c) computational mesh refined near coating and substrate interfaces.

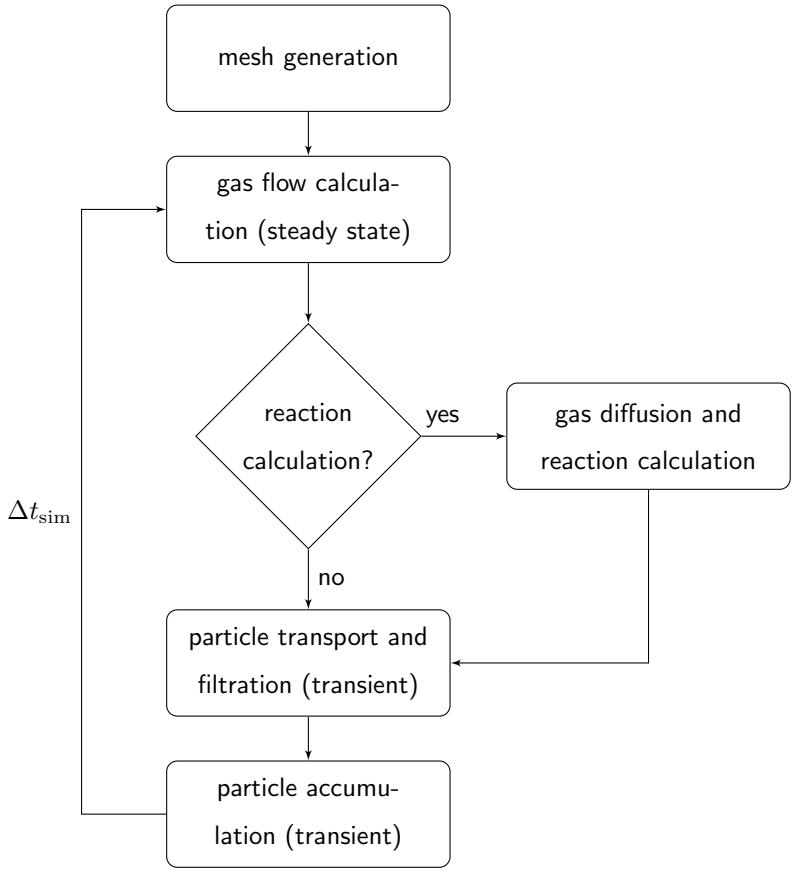

Figure 4: Block scheme of the proposed computational framework.

3.1. Model of gas flow

The fluid flow is assumed laminar and simulated in the whole domain simultaneously, including free pores, catalytic coating, and already accumulated particle deposits. For this purpose, the following variant of the Navier-Stokes equations for isothermal incompressible flow is considered,

$$\begin{aligned} \nabla \cdot (\boldsymbol{u} \otimes \boldsymbol{u}) - \nabla \cdot (\nu \nabla \boldsymbol{u}) &= -\nabla p + \boldsymbol{s} \\ \nabla \cdot \boldsymbol{u} &= 0 \,, \end{aligned} \tag{1}$$

where $\boldsymbol{u}$ corresponds to the fluid velocity, p to the kinematic pressure, and the coefficient ν denotes the fluid kinematic viscosity. Kinematic viscosity ν of the gas flowing through the filter wall is calculated from:

$$\nu = \frac{\mu}{\rho} \,, \quad \mu = \frac{bT^{3/2}}{T+S} \,, \tag{2}$$

where ρ is the fluid density computed from the ideal gas equation and μ stands for the dynamic viscosity given by the Sutherland equation (2), with the parameters $b = 1.458 \times 10^{-6}$ kg m^2 s^{-1} K$^{-1/2}$ and $S = 110.4$ K [36].

The additional source term $\boldsymbol{s}$ in equation (1) reflects the additional resistance to the flow present in the catalytic coating as well as in the formed particle deposits, which both possess internal porosity. This source term is based on the Darcy permeability model [37] and it is defined as

$$\boldsymbol{s} = \begin{cases} \mathbf{0} & \text{in} \quad \text{free pores} \\ -\varphi_{\mathrm{s}} \dfrac{\nu}{\kappa_{\mathrm{s}}} \boldsymbol{u} & \text{in} \quad \text{soot deposits} \\ -\dfrac{\nu}{\kappa_{\mathrm{c}}} \boldsymbol{u} & \text{in} \quad \text{coated zones} \,, \end{cases} \tag{3}$$

where κ_{s} and κ_{c} are the local Darcy permeabilities of the corresponding porous zones. The value of κ_{c} for the catalytic coating is estimated from the Carman-Kozeny equation [38] based on the porosity and characteristic diameter of particles forming the zone presented in [17] and the $\kappa_{\mathrm{c}} = 2.76 \times 10^{-15}$ m^2. The structural parameters of deposited soot and surrogate ZnO particles are provided in Table 1. In the first approximation, ZnO deposit permeability was set

Table 1: Structural parameters of the deposited soot and surrogate ZnO particles.

Parameter	Symbol	ZnO deposits	soot deposits
Particle size distribution	d_p	10–1000 nm, Figure 2	15–150 nm, Figure 5 [40]
Particle density	ρ_p	5600 $\mathrm{kg\,m^{-3}}$	1000 $\mathrm{kg\,m^{-3}}$ [41]
Deposit density	ρ_s	2800 $\mathrm{kg\,m^{-3}}$	90 $\mathrm{kg\,m^{-3}}$ [39]
Deposit porosity	ε_s	0.5	0.91
Deposit permeability	κ	7.69×10^{-14} $\mathrm{m^2}$	7.69×10^{-14} $\mathrm{m^2}$ [39]

to the same value as reported for the soot cake [39]. In order to account for a smooth and continuous growth of particle deposits, φ_s marks the actual local volume fraction of particle deposit in each finite volume cell, $\varphi_\mathrm{s} = V_\mathrm{s}/V_\mathrm{cell}$.

The boundary of the solution domain was divided in three sections (inlet, outlet and walls). At the inlet, we apply a uniform inlet velocity in the direction orthogonal to the wall (y axis) and a zero-gradient boundary condition for the pressure. At the outlet, constant pressure and so-called inlet-outlet boundary condition for $\boldsymbol{u}$ is used, which stabilises the calculation. No-slip boundary condition was specified at the walls.

Such defined mathematical model of flow was solved by the OpenFOAM toolbox [33], employing the porousSimpleFoam steady state solver that uses the consistent SIMPLE algorithm [42, 43] to compute the pressure-velocity coupling.

3.2. Model of particle movement

The particle movement model is based on Lagrangian tracking of individual spherical particles moving through the actual reconstructed 3D media [20]. Because the soot particles in the studied system are small and sparsely distributed, particle-particle interactions are neglected. The initial velocity of each particle entering the system is equal to gas velocity $u_{y,\mathrm{in}}$. The particle motion inside the system is governed by the Newton's second law,

$$\rho_\mathrm{p} V_\mathrm{p} \frac{\mathrm{d}\boldsymbol{u}_\mathrm{p}}{\mathrm{d}t} = \boldsymbol{F}_\mathrm{D} + \boldsymbol{F}_\mathrm{B}\,, \tag{4}$$

where m_p is mass of the particle and $\boldsymbol{u}_\mathrm{p}$ is its velocity. On the right hand side, $\boldsymbol{F}_\mathrm{D}$ and $\boldsymbol{F}_\mathrm{B}$ stand for the drag and the Brownian force, respectively, acting on the microscopic solid particle at the time t [20]. The laminar drag force $\boldsymbol{F}_\mathrm{D}$ is represented by the Stokes law taking into account the pre-calculated gas flow field $\boldsymbol{u}$,

$$\boldsymbol{F}_\mathrm{D} = \frac{3\pi\mu d_\mathrm{p}}{C_\mathrm{C}}(\boldsymbol{u} - \boldsymbol{u}_\mathrm{p})\,, \tag{5}$$

where d_p is the particle diameter and C_C is the Cunningham slip factor [44]

$$C_\mathrm{C} = 1 + \frac{2\lambda}{d_\mathrm{p}}\left[1.257 + 0.4\exp\left(-1.1\frac{d_\mathrm{p}}{2\lambda}\right)\right]\,. \tag{6}$$

The calculation of Brownian force utilizes the vector of zero-mean independent Gaussian random numbers of unit variance $\boldsymbol{G}$ [20],

$$\boldsymbol{F}_\mathrm{B} = \rho_\mathrm{p} V_\mathrm{p} \boldsymbol{G}\sqrt{\frac{\pi S_0}{\Delta t_\mathrm{p}}}, \quad \boldsymbol{G}(t) \in \mathbb{R}^3\,. \tag{7}$$

The variable S_0 is linked to the spectral intensity of the Gaussian white noise and provides the Brownian force amplitude [45],

$$S_0 = \frac{216\nu k_\mathrm{B} T}{\pi^2 \rho d_\mathrm{p}^5 \left(\frac{\rho_\mathrm{p}}{\rho}\right)^2 C_\mathrm{C}}\,, \tag{8}$$

where ρ and ρ_p are densities of the gas and particle, respectively. The integration step for particle movement solution according to equation (4) was 1×10^{-6} s, which was necessary for capturing the particle trajectory through the system including Brownian motion effects [20].

3.3. Particle deposition model

Particle trapping. In line with the clean filtration study [20], the probability of particle trapping is assumed $\mathcal{P} = 1$ upon particle-wall and particle-coating contact. To deal with the growing particle deposits, we must define also the probability of trapping in a cell that is partly occupied by the already accumulated particles. In the first approximation, this trapping probability corresponds to the volume fraction of deposits in the particular cell, $\mathcal{P} = \varphi_\mathrm{s}$. The test is

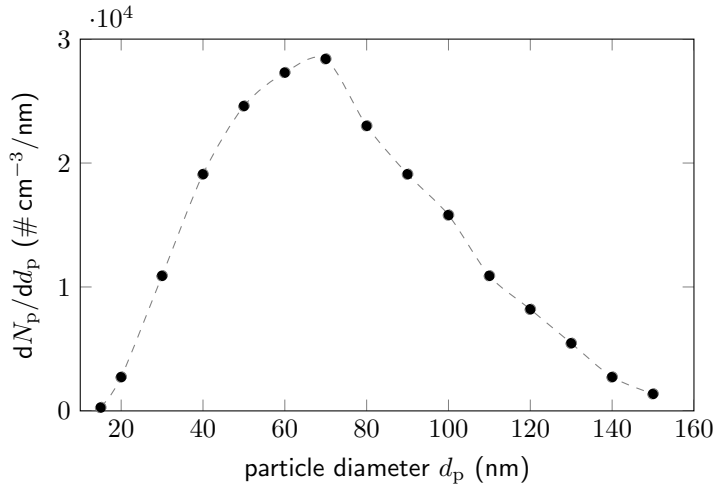

Figure 5: Gasoline soot particle size distribution used in the parametric simulation study of soot accumulation. Total concentration of particles was N_p =1×10^6 # cm^{-3}. Based on the data reported in [40].

implemented as a comparison of $\mathcal{P}$ with a randomly generated, uniformly distributed number. This test is performed for each particle just once in each cell on its trajectory. Once the particle is trapped, the corresponding increase in the local deposit volume is

$$\Delta V_\mathrm{s} = \frac{\rho_\mathrm{p}}{\rho_\mathrm{s}} V_\mathrm{p} = \frac{1}{1-\varepsilon_\mathrm{s}} V_\mathrm{p}\,, \tag{9}$$

where ρ_p and ρ_s are densities of a single particle and porous solid deposit, respectively, and ε_s is porosity of the deposit. The parameters of ZnO and soot particle deposits are summarized in Table 1. The considered particle size distributions of ZnO and soot are provided in Figure 2 and Figure 5, respectively.

The growth of particle deposits inevitably includes situations when the particles are trapped in almost fully occupied cell with $\varphi_\mathrm{s} \lesssim 1$ and adding the corresponding deposit volume would lead to $V_\mathrm{s} > V_\mathrm{cell}$, i.e., $\varphi_\mathrm{s} > 1$, which is physically unfeasible. To deal with this issue while keeping the particle mass and volume balance, a localised redistribution of trapped particles from the overloaded cells was developed.

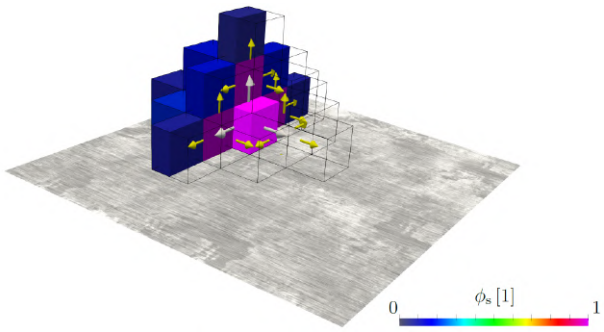

Figure 6: Expected behaviour of the particle deposit redistribution algorithm on walls. The fully occupied cells are magenta, the source cell is bright. The excess particle volume is redistributed in the direction of white arrows first and later in the direction of yellow arrows. The target cells are in blue-green color shades indicating lower volume fractions of particle deposits φ_s.

Particle deposit redistribution. The demands on particle redistribution model are as follows. First, the soot should be redistributed in a physically meaningful manner. Second, the algorithm needs to be computationally efficient, robust, and easily parallelized. Unfortunately, the aforementioned tasks seem to be anti-correlated.

The expected algorithm behaviour is demonstrated in Figure 6. The code needs to take into account a possibility of $\varphi_s > 1$ in a cell surrounded by cells in which $\varphi_s \geq 1$ already. Such a situation is shown in both Figures 6a and b. However, in Figure 6a, the source cell Ω_P with $\varphi_s > 1$ is placed on an impermeable wall and the soot is redistributed through all of its available face-neighbours. On the other hand, in Figure 6b the source cell lies on a pre-existing continuous layer of cells with $\varphi_s = 1$. Hence, the source cell face neighbour appertaining to the soot layer should not be used for the soot redistribution. However, the continuous soot layers are not easily identified.

This problem is mitigated by (i) redistributing the trapped particles between the cells via artificially-defined face fluxes, combined with (ii) a *tick-tock* approach to construction of these face fluxes for φ_s modification. Concentrating on the source cell Ω_P with $\varphi_{s,P} > 1$, in each odd step of the algorithm, only

the faces shared with the neighbouring cells $\Omega_N \in \{\Omega_N\}_P$ with $\varphi_{\mathrm{s},N} < 1$ are considered for particle deposit redistribution in such a manner that $\varphi_{\mathrm{s},P} = 1$ after the algorithm step. In each even algorithm step, the already exploited faces of the cell Ω_P are not re-used. But, if required, the previously unused faces shared with the neighbouring cells $\Omega_N \in \{\Omega_N\}_P$ having $\varphi_{\mathrm{s},N} \geq 1$ are utilised. This approach allows to increase the stencil available for the soot redistribution by one layer of cells each two algorithm iterations, while preserving the required algorithm behaviour. The developed algorithm for redistribution of the deposited particles was implemented in the OpenFOAM library and is available in a repository [46, 47].

Finally, after the simulated particle deposition period Δt_{sim}, the gas flow field is updated, reflecting the changed morphology of the porous structure, and the simulation continues in the loop as described in Figure 4. One possible strategy could be to adapt the value of Δt_{sim} for flow field recalculation according to the deposit growth rate, i.e., to trigger the flow field recalculation only after a significant increase in the deposit volume. However, for the case of low filtration efficiency and/or low inlet concentration of particles, this would result in an extremely long Δt_{sim}. In combination with the fixed internal time-step of 1×10^{-6} s in the particle movement simulation, this would lead to computationally expensive simulations.

To make the computation faster, we propose an alternative approach. The growth of particle deposits is simulated at a virtually increased particle concentration $N_{\mathrm{p,sim}}$ in the inlet gas, leading to an accelerated soot loading compared to the real particle concentration $N_{\mathrm{p,real}}$, Table 2. The acceleration factor is

$$\frac{\Delta t_{\mathrm{real}}}{\Delta t_{\mathrm{sim}}} = \frac{N_{\mathrm{p,sim}}}{N_{\mathrm{p,real}}}\,. \tag{10}$$

For example, when using ten times higher inlet concentration of particles, the simulated particle deposition process is ten times faster than in reality. The filtration efficiency increases from bare filter samples to the filters with catalytic coating, with the on-wall coated samples typically exhibiting the highest filtration efficiency [20]. The values of $N_{\mathrm{p,sim}}$ in Table 2 reflect this trend. The initial

Table 2: Simulation parameters for transient particle deposition.

Sample	$N_{\mathrm{p,real}}$ ($\#\,\mathrm{cm}^{-3}$)	$N_{\mathrm{p,sim}}$ ($\#\,\mathrm{cm}^{-3}$)	Δt_{sim} (s)	Δt_{real} (s)
BF0 – ZnO	1.9×10^{9}*	1.90×10^{10}*	0.5	5
BF1 – soot	1×10^{6}	2.74×10^{10}	0.5	13700
CF1 – soot	1×10^{6}	3.42×10^{9}	0.5	1710
CF2 – soot	1×10^{6}	1.71×10^{9}	0.5	856
CF3 – soot	1×10^{6}	8.55×10^{8}	0.5	428

* The number concentrations of ZnO particles $N_{\mathrm{p,real}}$ increased five times during the initial 10 s of the experiment; $N_{\mathrm{p,sim}}$ was adjusted accordingly.

estimates of $N_{\mathrm{p,sim}}$ were set according to the expected deposit formation rate in each sample based on the initially simulated clean filtration efficiency and, if necessary, revised after few time steps of transient accumulation simulation. The final $N_{\mathrm{p,sim}}$ values used in the simulations are provided in Table 2.

With this strategy, it was possible to keep a constant flow recalculation time-step $\Delta t_{\mathrm{sim}} = 0.5$ s in all simulations. Note that this time step is still an order of magnitude longer than the mean residence time of gas in the wall (ca. 0.02 s at $u_{y,\mathrm{in}} = 0.01\ \mathrm{m\,s}^{-1}$), thus providing a sufficient period for transient particle trapping simulation. The time evolution of particle deposits obtained from the accelerated simulation was then scaled back to the real particle concentration using equation (10). The real concentration of surrogate ZnO particles in the validation experiment, $N_{\mathrm{p,real}}$ in Table 2, was obtained by integrating the measured particle size distribution, Figure 2. The soot particle concentration $N_{\mathrm{p,real}}$ for the subsequent parametric simulation study was set to $10^{6}\ \#\,\mathrm{cm}^{-3}$, which is within the reported span for gasoline engines [48, 13].

4. Results

4.1. Model validation

A time-resolved XRT experiment during the filtration process, described in Section 2, was used for the model validation, considering ZnO particle size distribution presented in Figure 2. The ZnO particle density is higher than that of

soot particle, Table 1. This is accounted for in the model as the particle density is one of the input parameters used for the calculation of particle momentum and related forces during the filtration simulation, see equations (4), (7) and (8).

The predicted evolution of particle deposits is visualised in Figure 7, where the model predictions are compared to the experimental observation from XRT scans. For the visualisation of particle deposits in the simulations, the cells occupied by more than 10% (i.e., with local volume fraction $\varphi_{\mathrm{s},P} > 0.1$) are displayed in red colour. Note that the smallest deposits are not detected by the XRT due to de-noising and threshold algorithms that must be applied to avoid artefacts. Thus, the experimental data show only larger domains of aggregated particles. Nevertheless, it can be seen that the location and dynamics of the deposits formation in the simulation and experiment correspond reasonably well. Most of the particles are captured in the top part of the wall, but some of them penetrate deep into the wall.

This is further quantified by the averaged 1D profiles of the deposited particles through the the filter wall in Figure 8. The coordinate y corresponds to the top-down direction in Figure 7, and at each y location the averaging was performed over the entire xz plane (represented by a slice of the computational mesh cells). The external surface of wall is located near $y = 50\,\mu$m. The peak of captured particles exhibits its maximum ca 5-10 microns below the external surface, i.e., around $y = 55$–$60\,\mu$m. A considerable amount of particles still penetrate up to $30\,\mu$m deep inside the wall. Then there is a tail of deposits at much lower but still detectable amount up to $y = 145\,\mu$m, i.e., 95 microns deep into the wall. The relatively fast decrease of the particle volume fraction at that location suggests that there may be some pore neck or other morphological feature that prevents further penetration of particles. The deposits deeper in the wall ($y > 150\,\mu$m) are only minor.

Figure 8 confirms good overall agreement of the model predictions and XRT scan both in terms of spatial and temporal evolution. A minor difference (few microns) can be seen in the location of the peak near the wall entrance. The

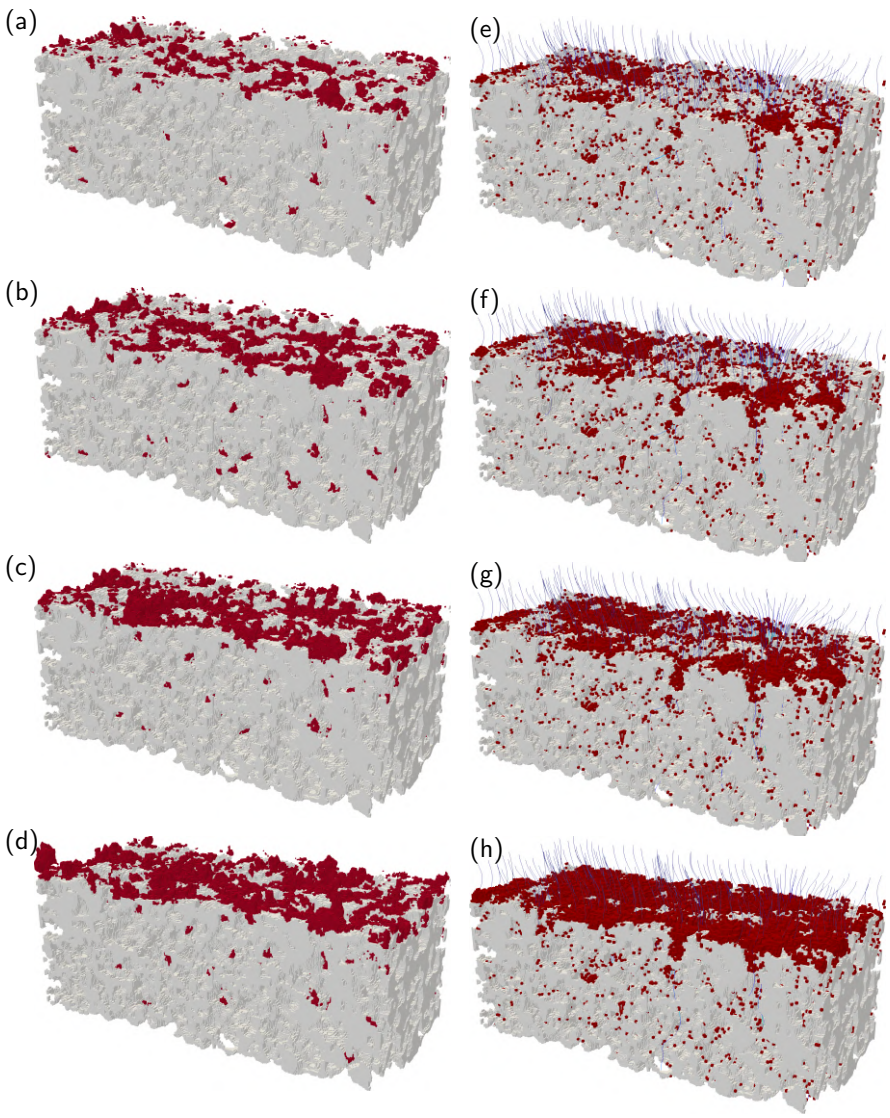

Figure 7: Evolution of particle deposits in a 3D reconstructed section of the BF0 filter wall as observed by time-resolved XRT during the experiment (a-d), and predicted by the simulation (e-h). Substrate = grey, particles = red, snapshot times $t = 10\,\mathrm{s}$ (a,e), $t = 30\,\mathrm{s}$ (b,f), $t = 50\,\mathrm{s}$ (c,g), and $t = 110\,\mathrm{s}$ (d,h).

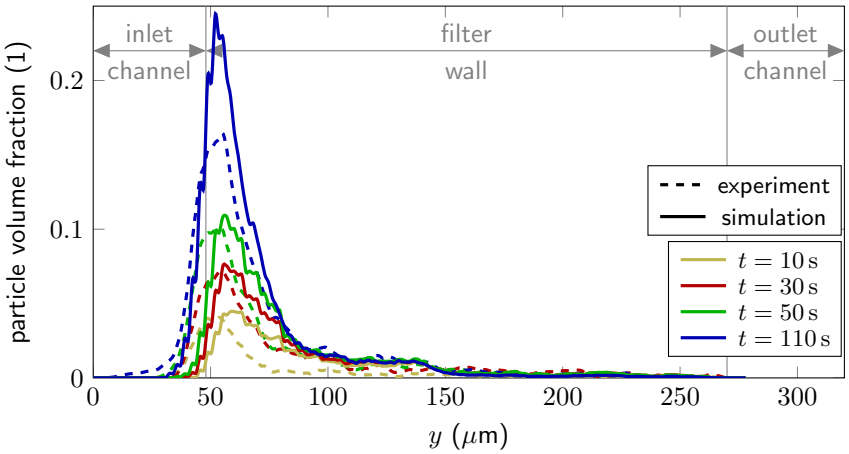

Figure 8: Averaged 1D profiles of the deposited particles over the filter wall during the filtration process. Comparison of model predictions and time-resolved XRT during the experiment.

model predicts slightly deeper penetration while the deposits by XRT are located more towards the external surface. The biggest difference is in the peak value at $t = 110\,\mathrm{s}$, where the model predicts much sharper peak compared to the XRT scan. This could be caused by the re-entrainment and secondary movement of particle agglomerates, which is not included in the model yet.

The reason for sudden decrease in the amount of deposited particles in the middle of the wall around $y = 145\,\mu\mathrm{m}$ is further explored in Figures 9–11. The xz slice through the wall at $y = 127\,\mu\mathrm{m}$ (i.e., $77\,\mu\mathrm{m}$ deep) shows a significant accumulation of particles in a pore located in the upper right quadrant, and another one in the lower right quadrant, with only minor contributions of other locations, Figure 9. The particle deposition regions predicted by the model agree reasonably well with the XRT observations during the filtration experiment. Deeper in the wall, Figure 10, the deposits are observed in the same xz locations, however, the corresponding pores get narrower, which is particularly visible for the pores in the upper right quadrant. Finally, Figure 11 shows the situation at $y = 174\ \mu\mathrm{m}$, which is ca. $124\ \mu\mathrm{m}$ deep inside the wall. Here the region in upper right quadrant shows only minimum deposited particles. This indicates that most of the particles were trapped in a narrower and more tortuous part

of the pores located above, cf. Figure 10. There are just two minor deposits in the lower right quadrant, the locations of which agree in the simulation and experiment. Considering the simplifying assumptions of the model as well as detection limits of the XRT, one cannot expect perfect voxel-to-voxel agreement between the simulation and experiment, nevertheless, Figures 8–11 demonstrate that the model is able to predict correctly the locations of increased particle accumulation in 3D structure of the filter wall.

4.2. Coating location parametric study

The validated model was subsequently used in a simulation study of the catalytic coating location influencing the filtration process. The samples CF1, CF2 and CF3 have similar amount of coating but different location, while the sample BF1 is a bare substrate structure obtained by virtually removing the catalytic coating from the sample CF1. Soot particle size distribution used in this study is described in Figure 5 with the related parameters provided in Tables 1 and 2. The soot accumulation simulations are computed at the superficial gas velocity through wall $u_{y,\mathrm{in}} = 0.01\,\mathrm{m\,s^{-1}}$ at temperature 453 K.

Figure 12 compares the samples BF1, CF1, CF2, CF3 in terms of their wall microstructure (a-d) as well as the distribution of soot deposits formed before reaching the filtration efficiency 99.9% (e-h). The clean filtration efficiency of all samples is lower than that, which means that open pathways through the wall pores must have been closed (at least locally) by the deposited soot in order to reach the nearly complete filtration efficiency. This process took a different amount of time for each sample as will be discussed in more detail later.

The bare substrate BF1 had to accumulate the highest amount of soot and the soot particles penetrated the whole wall, Figure 12e. In contrast, the in-wall coated sample CF1 with the identical substrate structure needs a significantly lower amount of soot deposits to reach the complete filtration efficiency, Figure 12f. This is in line with the reduced volume of the wall pores that are partly occupied by the coated catalyst. Still, a relatively large part of soot penetrated inside the wall structure, particularly in the pathway of the largest

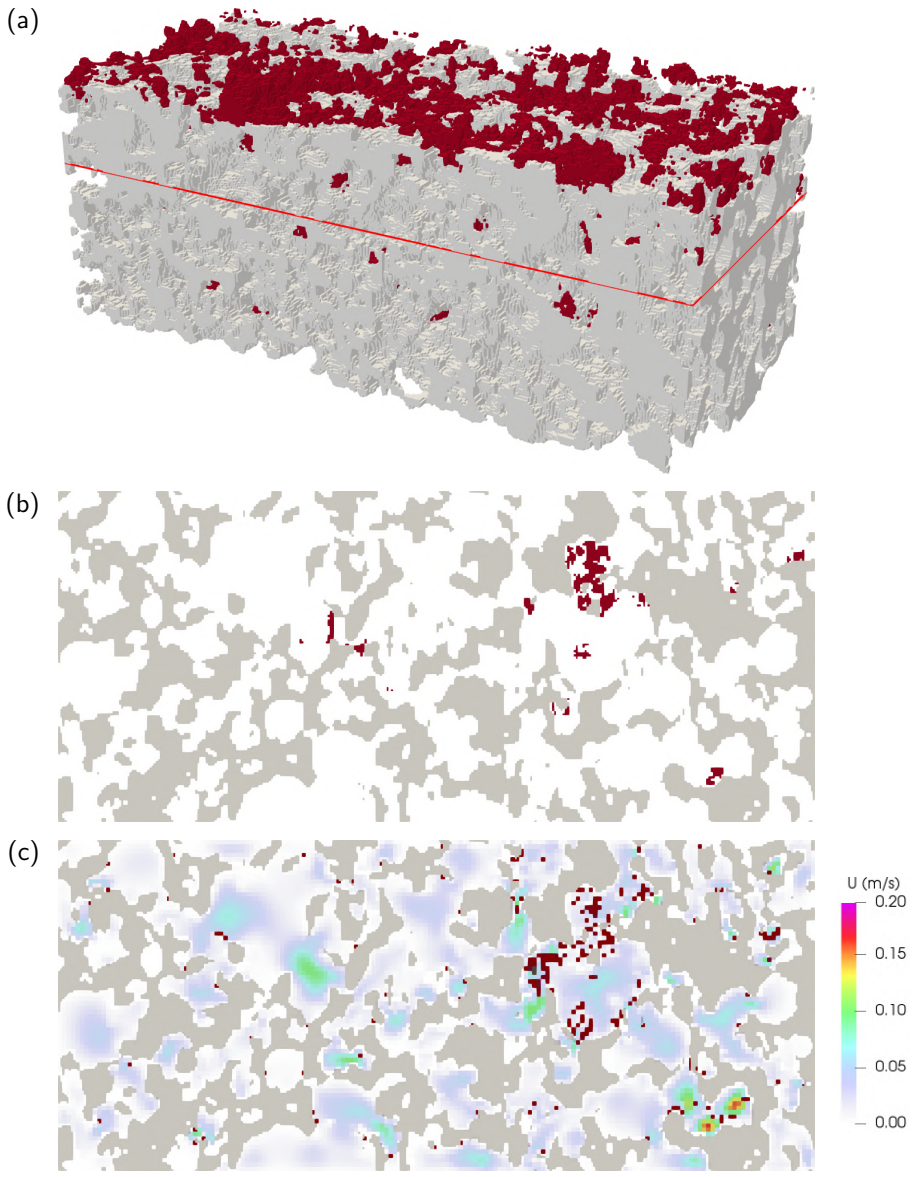

Figure 9: Comparison of the predicted and scanned particle deposits for time 50 s at y = 127 μm, which is ca. 77 μm deep inside the wall: a) wall section with the marked slice location, b) deposits in the slice as seen in the segmented XRT scan, c) deposits and local gas velocity magnitude predicted by the simulation. Deposited particles = red, substrate = grey.

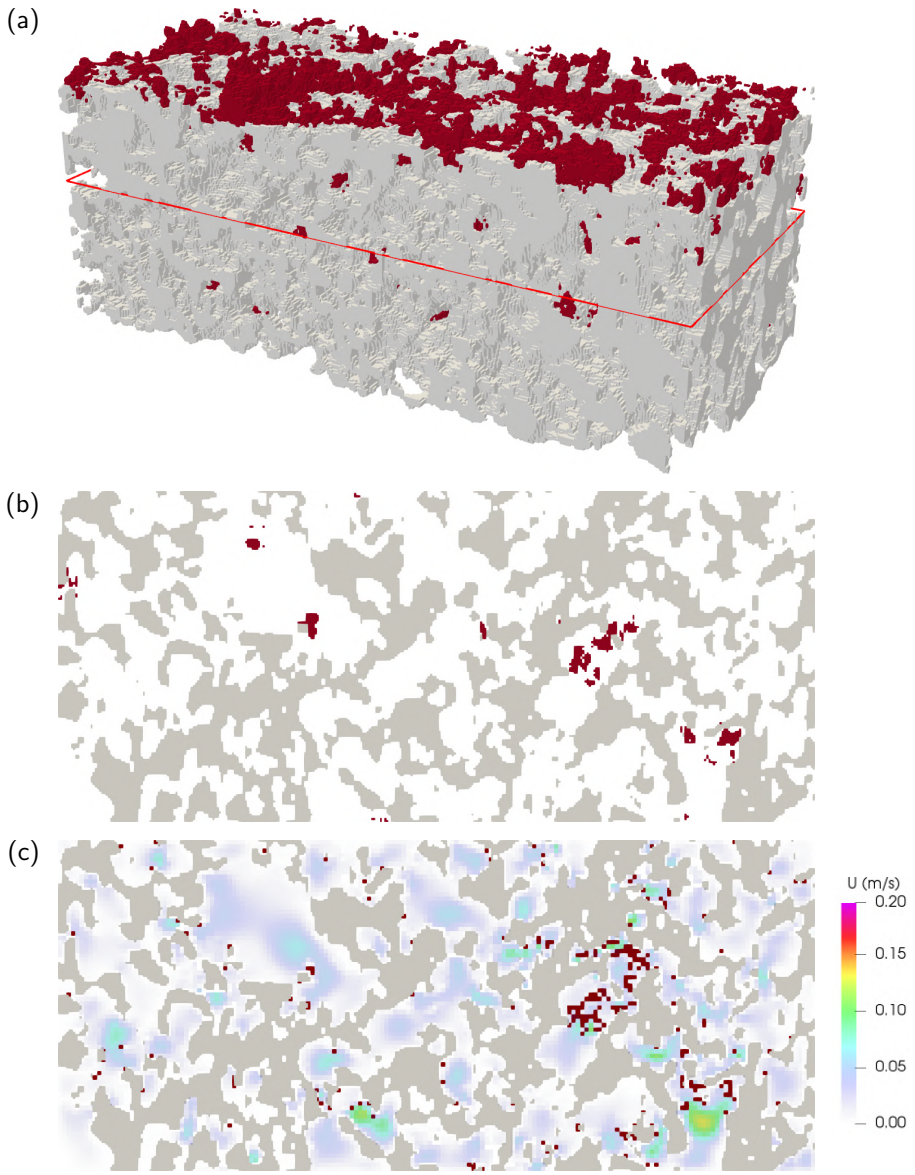

Figure 10: Comparison of the predicted and scanned particle deposits for time 50 s at $y = 143\,\mu$m, which is ca. $93\,\mu$m deep inside the wall: a) wall section with the marked slice location, b) deposits in the slice as seen in the segmented XRT scan, c) deposits and local gas velocity magnitude predicted by the simulation. Deposited particles = red, substrate = grey.

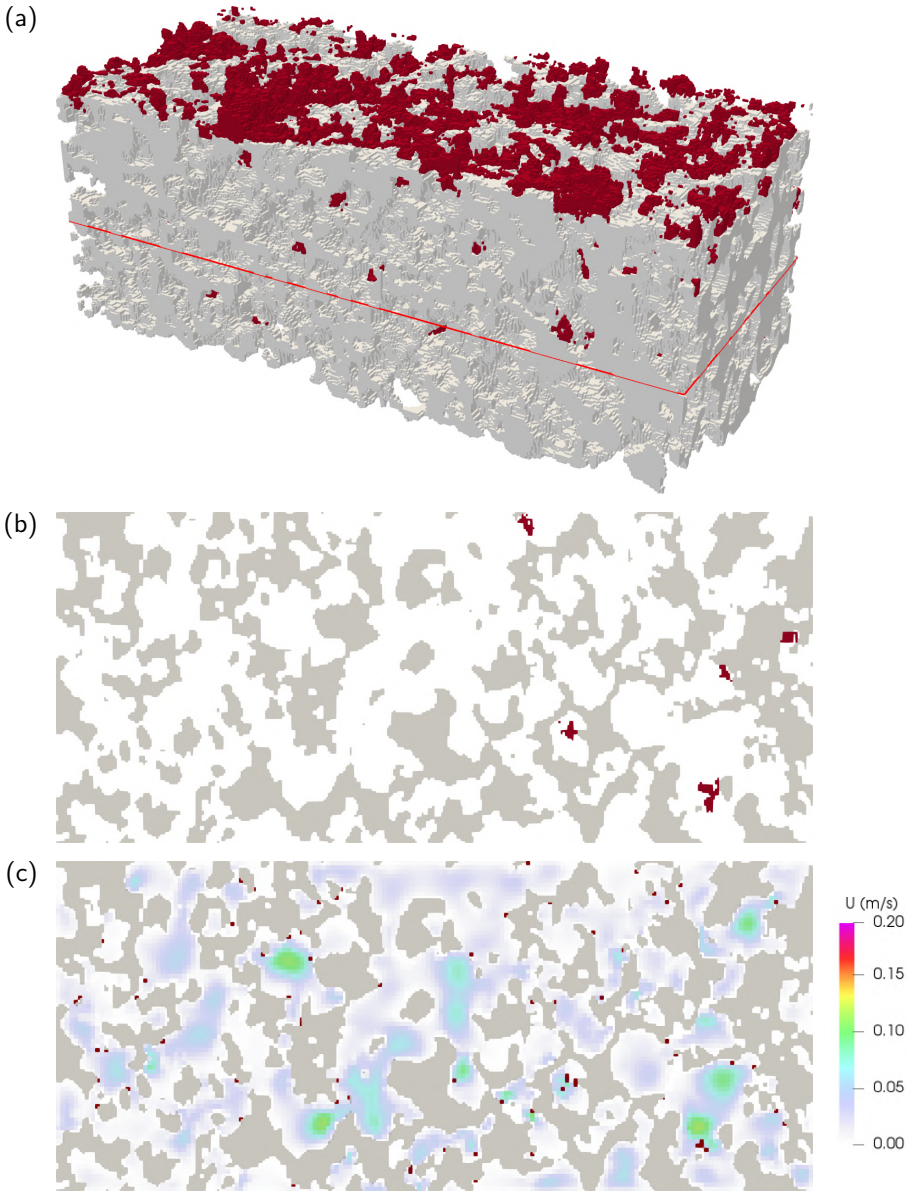

Figure 11: Comparison of the predicted and scanned particle deposits for time 50 s at $y = 174\,\mu$m, which is ca. $124\,\mu$m deep inside the wall: a) wall section with the marked slice location, b) deposits in the slice as seen in the segmented XRT scan, c) deposits and local gas velocity magnitude predicted by the simulation. Deposited particles = red, substrate = grey.

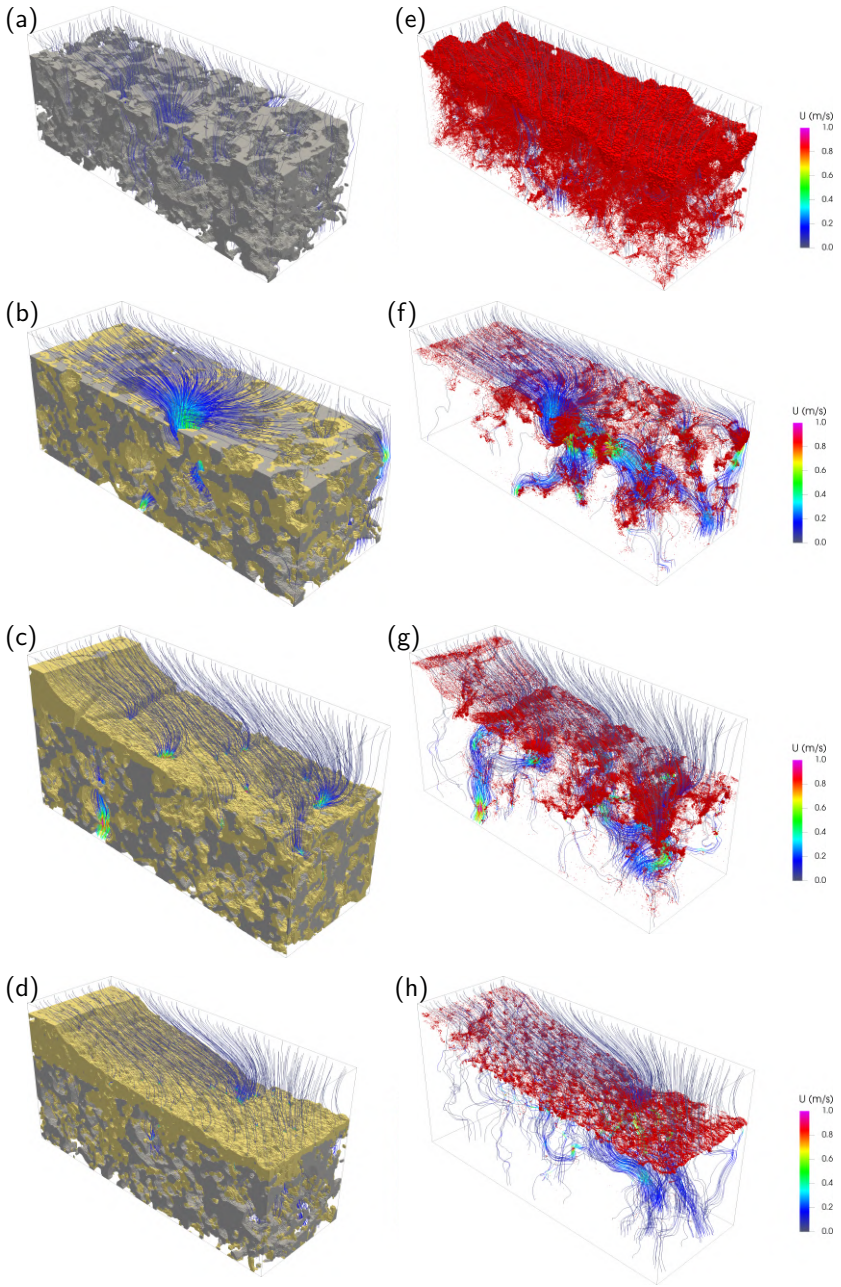

Figure 12: 3D reconstructed section of filter wall with gas streamlines for samples BF1, CF1, CF2, CF3 (a-d), and soot deposits with local volume fraction $\varphi_{s,P} > 0.1$ after reaching the filtration efficiency 99.9% (e-h). Substrate = grey, catalytic coating = yellow, particles = red, sample BF1 (bare) (a,e), CF1 (in-wall) (b,f), CF2 (combined) (c,g), and CF3 (on-wall) (d,h).

permeating pore in the middle of the reconstructed section, as indicated by the gas streamlines.

The sample CF2 with part of the coating located on top of the wall shows a reduced soot penetration depth, Figure 12g. Though there are still few dominant permeation pathways, they lead mostly through the cracks and other imperfections in the coated layer on top of the wall. These narrower passages are soon closed by the soot deposits and the deep bed filtration is finished. The sample CF3 with a continuous layer of the catalyst on top of the wall shows

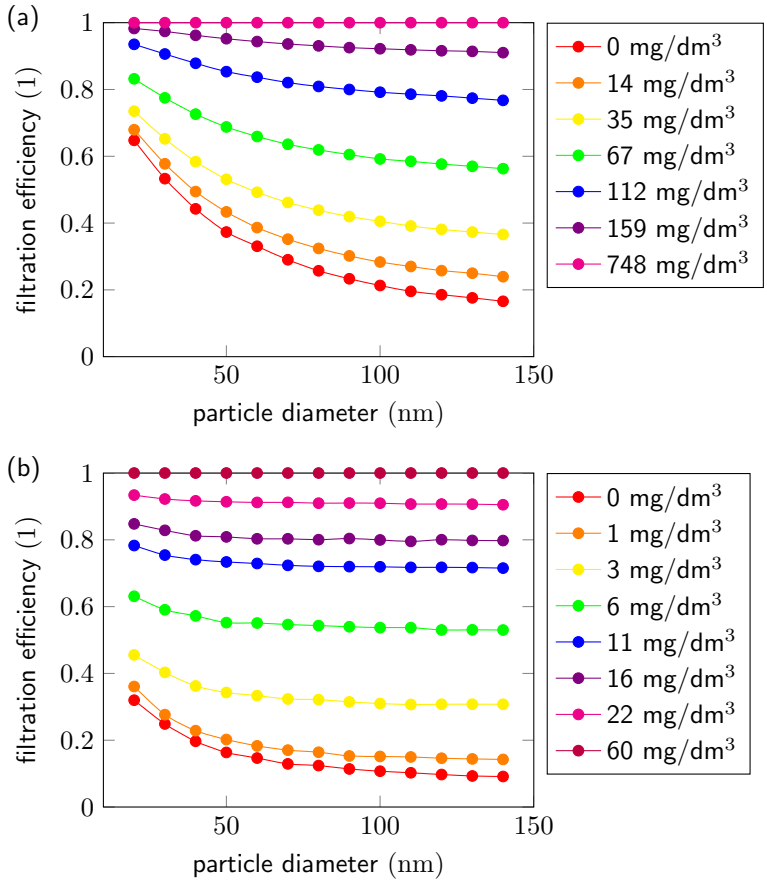

Figure 13: Predicted evolution of filtration efficiency dependency on particle diameter with increasing soot deposit volume in whole filter: a) the sample BF1 (bare substrate), b) the sample CF1 (catalytic coating in the wall).

practically no penetration of soot and the deposits remain on the external surface, Figure 12h. In this case, just a little amount of soot is needed to reach the complete filtration efficiency.

The predicted evolution of filtration efficiency depending on the soot particle diameter and the accumulated soot mass is shown in Figure 13 and Figure 14. For the soot particles around 100–200 nm, direct interception is the dominant filtration regime and the efficiency does not depend much on the particle diameter. On the other hand, filtration efficiency of the smaller particles grows

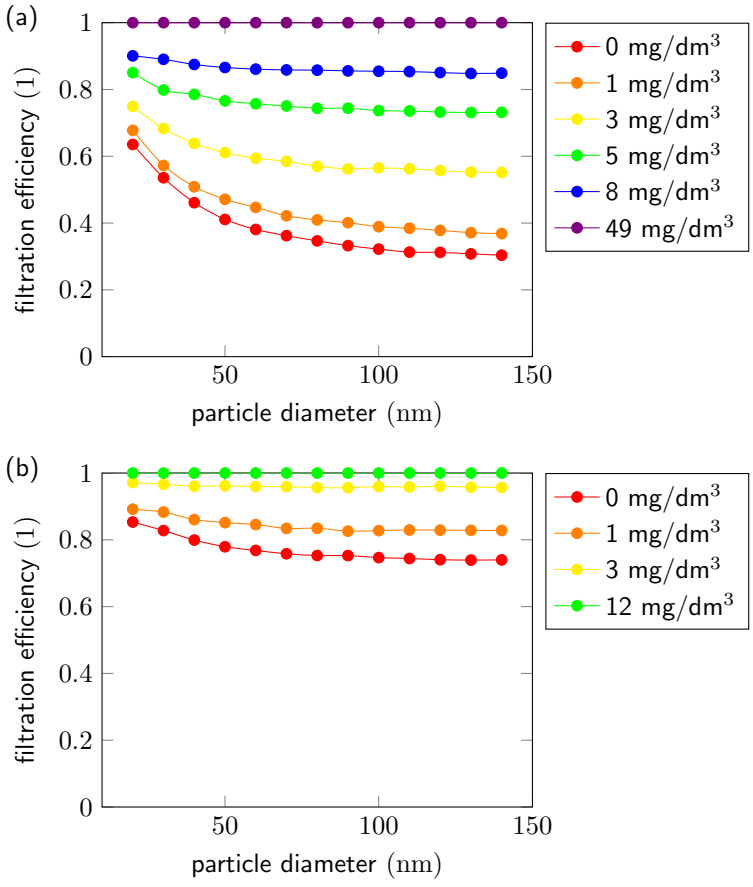

Figure 14: Predicted evolution of filtration efficiency depending on particle diameter with increasing soot deposit volume in whole filter: a) the sample CF2 (catalytic coating combination in & partly on the wall), b) the sample CF3 (catalytic coating mainly on the wall).

due to increasing impact of Brownian motion [20]. The accumulated soot mass is recalculated from the simulated microscopic section of the wall to the volume of the whole monolith, using the wall thickness and channel density values provided in Section 2.

Somewhat counter-intuitively, the clean filtration efficiency of the bare sample BF1 is slightly higher then that of CF1 with the in-wall catalyst coating, Figure 13. This phenomenon was already reported before [24, 49] and is explained as follows. As a certain part of the wall pores is blocked by the coating, the local gas flow rate in the remaining free pores is higher, which may slightly decrease the filtration efficiency. However, during the filtration process, the sample CF1 shows much faster formation of soot cake than BF1 and its filtration efficiency increases more quickly with the deposited soot mass, Figure 13. The amount of deposited soot required to reach the complete filtration efficiency in the coated sample CF1 is more than ten times lower than in the bare filter BF1.

The initial clean filtration efficiency increases with the catalytic coating located in the on-wall layer, see the results for the samples CF2 and CF3 in Figure 14. Co-currently, the deposited soot mass required to reach the complete filtration efficiency decreases, which means that the whole process becomes much faster.

Figure 15 compares the transient evolution of average filtration efficiency for all the studied samples. The sample CF3 with a continuous catalyst layer on top of the wall reaches the complete filtration efficiency within 15 minutes of its operation. The sample CF2 with non-compact catalytic layer on the wall requires 85 minutes of soot accumulation, and the sample CF1 with just the in-wall catalyst coating reaches the full filtration efficiency after 4 hours. The bare sample BF1 needs much more time on stream and, though its initial filtration efficiency is higher than that of CF1, reaches the efficiency of 99.9% only after more than 60 hours of operation, which makes it unacceptable for the real operation.

The corresponding evolution of pressure drop over the wall of the individual

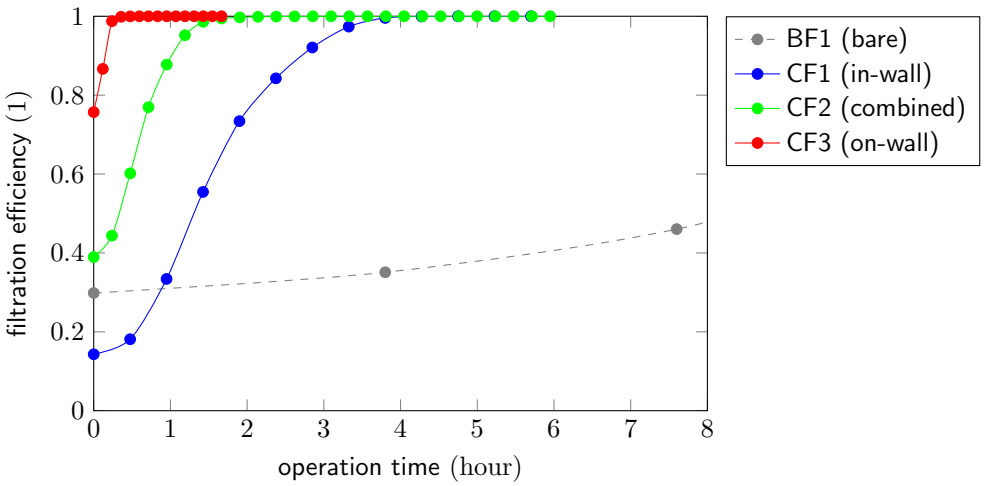

Figure 15: Predicted average filtration efficiency evolution for the samples with different distribution of catalytic coating.

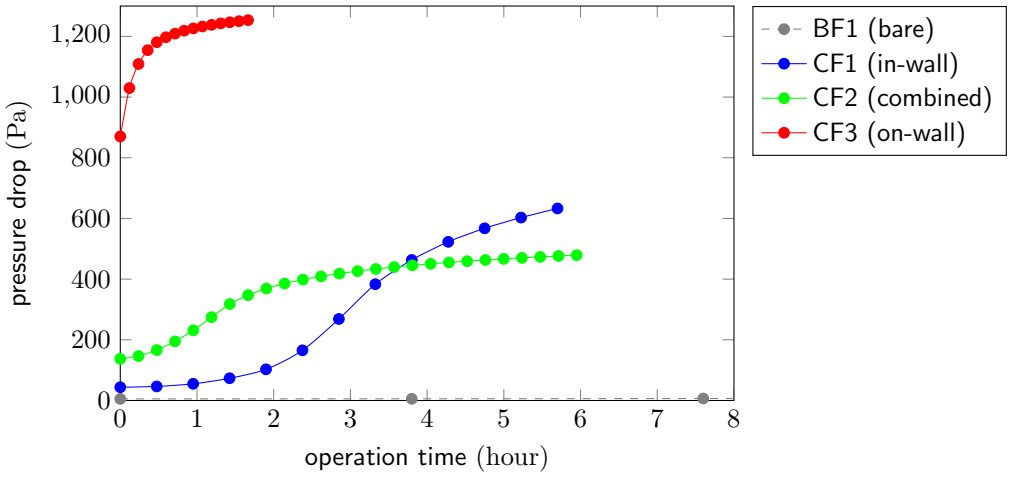

Figure 16: Predicted wall pressure drop evolution for the samples with different distribution of catalytic coating.

samples is shown in Figure 16. Note that the pressure drop of the whole filter consists of contraction/expansion effects at the channel inlet/outlet, friction along the channel, and pressure drop over the wall [21]. The micro-scale model used in this simulation study accounts just for the evolution of the latter contribution. With a relatively thin cake, the other two contributions remain similar to the clean filter and the computed evolution of wall pressure drop represents well the overall change. However, when the on-wall cake gets thick and occupies a significant part of the channel cross-section, the pressure drop at the channel inlet as well as the friction along the channel start to contribute to the increase of pressure drop. Modelling of this impact is out of the scope of this paper and we focus solely on the pressure drop over the wall.

Figure 16 reveals that the superior clean filtration efficiency of the sample CF3 with a continuous catalytic layer on top of the wall is accompanied by high initial pressure drop, which further increases during soot accumulation. The slope of pressure drop curve is quite steep from the beginning but gradually decreases and becomes significantly milder after 15 minutes, indicating transition from deep bed to cake filtration regime. After ca. 1 hour, the slope stabilizes and pressure drop increase of CF3 becomes linear as expected in a fully developed cake filtration.

The combined sample CF2 possesses cracks and local openings in its thinner on-wall layer, which significantly decreases the initial pressure drop in comparison to the uniform layer of coating present in the sample CF3, Figure 16. The soot accumulation period needed to close the open pathways in the wall and reach the complete filtration efficiency is longer for CF2, but the final pressure drop after transition to the cake filtration regime is approximately 65% lower than in CF3. The final slopes of the pressure drop increase in CF2 and CF3 are similar, confirming the transition to cake filtration regime.

The sample CF1 with the catalyst deposited only inside the wall exhibits the lowest initial pressure drop from the three coated samples. There is also a significant lag in the CF1 pressure drop increase after the start of the filtration process – almost no change in pressure can be seen within the first hour

of operation, Figure 16. This is caused by the relatively low clean filtration efficiency and large open pores present in the CF1 structure. It takes a considerable amount of time to build a significant deposits in the CF1 wall pores before they start to affect the pressure drop. When the CF1 pressure drop evolution is compared to the corresponding filtration efficiency curve in Figure 15, it can be concluded that the effect of the deposited soot on the filtration efficiency is immediate, while the impact on pressure drop develops with a certain delay. On the other hand, when the pressure drop starts to grow, its slope is quite high and continues even after 4 hours of operation, when the complete filtration efficiency has been reached. This indicates ongoing deep bed filtration regime with filling the wall pores by the deposited soot. The cake filtration regime, with a milder slope and linear pressure drop curve is reached only after more than 6 hours of operation. The extensive deep filtration period of the sample CF1 leads to a noticeably higher final pressure drop compared to the sample CF2 with the partial on-wall coating that speeds up the transition to cake filtration regime. The sample CF2 thus outperforms CF1 not only in terms of filtration efficiency but also when comparing the pressure drop after soot loading; the benefit of the low initial pressure drop of CF1 is lost during the filtration process, Figure 15.

5. Conclusions

The developed pore-scale model of particle deposition in the filter wall structure was first validated against time-resolved X-Ray tomography data acquired during the filtration experiment. The validated model was then used for simulations of soot deposition in different filter structures utilizing the same cordierite substrate with different distribution of catalytic coating.

The results revealed that the best trade-off between high filtration efficiency and low pressure drop can obtained with a combined catalytic coating located both inside and on top of the filter wall. The sample CF3 with practically all catalyst on top of the wall provided an excellent clean filtration efficiency but unacceptably high pressure drop. The sample CF1 coated only inside the wall

provided the lowest initial pressure drop, however, it increased significantly with time on stream as a result of deep filtration. The sample CF2, possessing part of the catalytic material in a thin catalytic layer on top of the wall, showed much faster transition to the cake filtration regime, leaving the wall pores free and achieving lower pressure drop after soot loading.

The particle accumulation model presented in this paper together with the convection-reaction-diffusion model for catalyzed reactions of gaseous pollutants [17] represent a powerful toolbox for further tuning of catalyst distribution on/in the filter wall. These simulation tools help to reach the ultimate goal for the practical application – the development of microstructures with optimum performance over the whole operating cycle of a catalytic filter.

Acknowledgments

The work has been financially supported by the Czech Science Foundation (GA 22-12227S). Martin Isoz gratefully acknowledges the institutional support RVO:61388998.

6. Nomenclature

b	Sutherland equation parameter, $\mathrm{kg\,m^2\,s^{-1}\,K^{-1/2}}$
d	diameter, m
F	force, N
m	mass, kg
N	number concentration, $\mathrm{\#\,m^{-3}}$
$\mathcal{P}$	probability of particle trapping, 1
p	pressure, Pa
S	Sutherland equation parameter, K
T	temperature, K
t	time, s
u	linear velocity, $\mathrm{m\,s^{-1}}$
x	spatial coordinate perpendicular to the flow direction, m

y	spatial coordinate in the flow direction, m

Greek letters

ε	porosity, 1
φ	volume fraction, 1
κ	Darcy's permeability, m^2
μ	dynamic viscosity, $\mathrm{Pa\,s}$
ν	kinematic viscosity, $\mathrm{m}^2\,\mathrm{s}^{-1}$
Ω	computational domain
Ω_P	cell in computational domain
Ω_N	face-neighbour of Ω_P
ρ	density, $\mathrm{kg\,m}^{-3}$

Subscripts and superscripts

B	Brownian
c	coated catalyst (porous)
D	drag
in	inlet
p	particle
s	soot deposit (porous)

Abbreviations

CFD	computational fluid dynamics
DPF	diesel particulate filter
GPF	gasoline particulate filter
LBM	Lattice Boltzmann method
MIP	mercury intrusion porosimetry
PF	particulate filter
PM	particulate matter
XRT	X-ray (micro)tomography

References

[1] C.A. Pope, N. Coleman, Z.A. Pond, and R.T. Burnett. Fine particulate air pollution and human mortality: 25+ years of cohort studies. *Environmental Research*, 183, 2020. doi: 10.1016/j.envres.2019.108924.

[2] Jinyoung Ko, Kangjin Kim, Wonyong Chung, Cha-Lee Myung, and Simsoo Park. Characteristics of on-road particle number (pn) emissions from a gdi vehicle depending on a catalytic stripper (cs) and a metal-foam gasoline particulate filter (gpf). *Fuel*, 238:363–374, 2019. doi: 10.1016/j.fuel.2018.10.091.

[3] CL Myung, A Ko, and Simsoo Park. Review on characterization of nanoparticle emissions and pm morphology from internal combustion engines: Part 1. *International Journal of Automotive Technology*, 15(2):203–218, 2014. doi: 10.1007/s12239-014-0022-x.

[4] Barouch Giechaskiel, Victor Valverde, Anastasios Kontses, Anastasios Melas, Giorgio Martini, Andreas Balazs, Jon Andersson, Zisis Samaras, and Panagiota Dilara. Particle number emissions of a euro 6d-temp gasoline vehicle under extreme temperatures and driving conditions. *Catalysts*, 11(5):607, 2021. doi: 10.3390/catal11050607.

[5] Jihwan Jang, Jongtae Lee, Yonghyun Choi, and Sungwook Park. Reduction of particle emissions from gasoline vehicles with direct fuel injection systems using a gasoline particulate filter. *Science of The Total Environment*, 644: 1418–1428, 2018. doi: 10.1016/j.scitotenv.2018.06.362.

[6] Christine Lambert, Timothy Chanko, Douglas Dobson, Xin Liu, and James Pakko. Gasoline particle filter development. *Emission Control Science and Technology*, 3(1):105–111, 2017. doi: 10.1007/s40825-016-0055-x.

[7] Heeje Seong, Seungmok Choi, Sungsik Lee, Nestor J Zaluzec, Todd J Toops, Michael J Lance, Daekun Kim, and Ke Nguyen. Deactivation of three-way catalysts coated within gasoline particulate filters by engine-oil-derived

chemicals. *Industrial & Engineering Chemistry Research*, 58(25):10724–10736, 2019. doi: 10.1021/acs.iecr.9b00342.

[8] Joerg Michael Richter, Raoul Klingmann, Stephanie Spiess, and Ka-Fai Wong. Application of catalyzed gasoline particulate filters to gdi vehicles. *SAE International Journal of Engines*, 5(3):1361–1370, 2012. doi: 10.4271/2012-01-1244.

[9] Matyáš Schejbal, J Štěpánek, Miloš Marek, P Kočí, and M Kubíček. Modelling of soot oxidation by no2 in various types of diesel particulate filters. *Fuel*, 89(9):2365–2375, 2010. doi: 10.1016/j.fuel.2010.04.018.

[10] Grigorios Koltsakis, Onoufrios Haralampous, Christopher Depcik, and J Colter Ragone. Catalyzed diesel particulate filter modeling. *Reviews in Chemical Engineering*, 29(1):1–61, 2013. doi: 10.1515/revce-2012-0008.

[11] ENRICO Tronconi, ISABELLA Nova, FABIO Marchitti, G Koltsakis, D Karamitros, B Maletic, N Markert, D Chatterjee, and M Hehle. Interaction of no x reduction and soot oxidation in a dpf with cu-zeolite scr coating. *Emission Control Science and Technology*, 1:134–151, 2015. doi: 10.1007/s40825-015-0014-y.

[12] Kenneth G Rappé. Integrated selective catalytic reduction–diesel particulate filter aftertreatment: Insights into pressure drop, no x conversion, and passive soot oxidation behavior. *Industrial & Engineering Chemistry Research*, 53(45):17547–17557, 2014. doi: 10.1021/ie502832f.

[13] Ameya Joshi and Timothy V Johnson. Gasoline particulate filters—a review. *Emission Control Science and Technology*, 4(4):219–239, 2018. doi: 10.1007/s40825-018-0101-y.

[14] M. Václavík, M. Plachá, P. Kočí, M. Svoboda, T. Hotchkiss, V. Novák, and D. Thompsett. Structure characterisation of catalytic particulate filters for automotive exhaust gas aftertreatment. *Materials Characterization*, 134: 311–318, 2017. doi: 10.1016/j.matchar.2017.11.011.

[15] Miroslav Blažek, Milan Žalud, Petr Kočí, Andrew York, Christian M Schlepütz, Marco Stampanoni, and Vladimír Novák. Washcoating of catalytic particulate filters studied by time-resolved x–ray tomography. *Chemical Engineering Journal*, 409:128057, 2021. doi: 10.1016/j.cej.2020.128057.

[16] Rudolf Pečinka, Miroslav Blažek, Richard Knopp, Petr Kočí, and Andrew York. Impact of diffusion limitations inside the wall of catalytic filters on conversion of gaseous pollutants at increased flow rates. *Chemical Engineering Science*, 260:117876, 2022. ISSN 0009-2509. doi: 10.1016/j.ces.2022.117876.

[17] Petr Kočí, Martin Isoz, Marie Plachá, Adéla Arvajová, Marek Václavík, Miloš Svoboda, Emily Price, Vladimír Novák, and David Thompsett. 3d reconstruction and pore-scale modeling of coated catalytic filters for automotive exhaust gas aftertreatment. *Catalysis Today*, 320:165–174, 2019. doi: 10.1016/j.cattod.2017.12.025.

[18] R. Greiner, T. Prill, O. Iliev, B. van Setten, and M. Votsmeier. Tomography based simulation of reactive flow at the micro-scale: Particulate filters with wall integrated catalyst. *Chemical Engineering Journal*, 378:121919, 2019. ISSN 1385-8947. doi: 10.1016/j.cej.2019.121919.

[19] J. Němec, M. Plachá, and P. Kočí. Effective modeling of coupled reaction and transport inside the catalytic filter wall. *Chemical Engineering Journal*, 461:141847, 2023. ISSN 1385-8947. doi: 10.1016/j.cej.2023.141847.

[20] M. Plachá, P. Kočí, M. Isoz, M. Svoboda, E. Price, D. Thompsett, K. Kallis, and A. Tsolakis. Pore-scale filtration model for coated catalytic filters in automotive exhaust gas aftertreatment. *Chemical Engineering Science*, 226, 2020. doi: 10.1016/j.ces.2020.115854.

[21] M. Leskovjan, J. Němec, M. Plachá, P. Kočí, M. Isoz, M. Svoboda, V. Novák, E. Price, and D. Thompsett. Multiscale modeling and analysis of pressure drop contributions in catalytic filters. *Industrial & Engineering Chemistry Research*, 60:6512–6524, 2021. doi: 10.1021/acs.iecr.0c05362.

[22] Igor Belot, David Vidal, Martin Votsmeier, Robert E Hayes, and Francois Bertrand. Numerical investigation of the impact of washcoat distribution on the filtration performance of gasoline particulate filters. *Chemical Engineering Science*, 221:115656, 2020. doi: 10.1016/j.ces.2020.115656.

[23] I. Belot, D. Vidal, R. Greiner, M. Votsmeier, R.E. Hayes, and F. Bertrand. Impact of washcoat distribution on the catalytic performance of gasoline particulate filters as predicted by lattice Boltzmann simulations. *Chemical Engineering Journal*, 406:127040, 2021. doi: 10.1016/j.cej.2020.127040.

[24] Xiangxiao Kong, Kerry Chen, Robert Greiner, Martin Votsmeier, Igor Belot, David Vidal, François Bertrand, Robert E Hayes, and Jason S Olfert. Particle size-dependent filtration efficiency and pressure drop of gasoline particle filters with varying washcoat volumes. *Emission Control Science and Technology*, pages 1–12, 2021. doi: 10.1007/s40825-021-00193-3.

[25] Zhijun Li, Fangchao Yan, Xiangjin Kong, Boxi Shen, Zhiyang Li, and Yan Wang. Simulation of soot particle deposition inside porous walls based on lattice boltzmann method for diesel particulate filter. *Journal of Environmental Chemical Engineering*, 9(4):105396, 2021. doi: 10.1016/j.jece.2021.105396.

[26] Kazuhiro Yamamoto and Shota Yagasaki. Numerical simulation of particle-laden flow and soot layer formation in porous filter. *Solids*, 3(2):282–294, 2022. doi: 10.3390/solids3020020.

[27] Matthew P Jones, Malte Storm, Andrew PE York, Timothy I Hyde, Gareth D Hatton, Alex G Greenaway, Sarah J Haigh, and David S Eastwood. 4d in-situ microscopy of aerosol filtration in a wall flow filter. *Materials*, 13(24):5676, 2020. doi: 10.3390/ma13245676.

[28] Robert C Atwood, Andrew J Bodey, Stephen WT Price, Mark Basham, and Michael Drakopoulos. A high-throughput system for high-quality tomographic reconstruction of large datasets at diamond light source. *Philosoph-*

ical Transactions of the Royal Society A: Mathematical, Physical and Engineering Sciences, 373(2043):20140398, 2015. doi: 10.1098/rsta.2014.0398.

[29] Nghia T Vo, Robert C Atwood, and Michael Drakopoulos. Superior techniques for eliminating ring artifacts in x-ray micro-tomography. *Optics express*, 26(22):28396–28412, 2018. doi: 10.1364/OE.26.028396.

[30] Nghia T Vo, Robert C Atwood, and Michael Drakopoulos. Radial lens distortion correction with sub-pixel accuracy for x-ray micro-tomography. *Optics express*, 23(25):32859–32868, 2015. doi: 10.1364/OE.23.032859.

[31] Caroline A Schneider, Wayne S Rasband, and Kevin W Eliceiri. Nih image to imagej: 25 years of image analysis. *Nature methods*, 9(7):671–675, 2012. doi: 10.1038/nmeth.2089.

[32] Johannes Schindelin, Ignacio Arganda-Carreras, Erwin Frise, Verena Kaynig, Mark Longair, Tobias Pietzsch, Stephan Preibisch, Curtis Rueden, Stephan Saalfeld, Benjamin Schmid, et al. Fiji: an open-source platform for biological-image analysis. *Nature methods*, 9(7):676–682, 2012. doi: 10.1038/nmeth.2019.

[33] C. Greenshields. *OpenFOAM v10 User Guide*. The OpenFOAM Foundation, London, UK, 2022. URL `https://doc.cfd.direct/openfoam/user-guide-v10`.

[34] David R. Snelling, Gregory J. Smallwood, Robert A. Sawchuk, Stuart W. Neill, Daniel Gareau, Daniel J. Clavel, Wallace L. Chippior, Fengshan Liu, and Ömer L. Gülder. In-situ real-time characterization of particulate emissions from a diesel engine exhaust by laser-induced incandescence. *SAE Technical Paper Series*, 2000-01-1994:1–13, 2000. doi: 10.4271/2000-01-1994.

[35] Said Elgobashi. On predicting particle-laden turbulent flows. *Applied Scientific Research*, 52:309–329, 1994. doi: 10.1007/BF00936835.

[36] W Sutherland. The viscosity of gases and molecular force. *Lond. Edinb. Dublin Philos. Mag. J. Sci*, 36:507–531, 1893. doi: 10.1080/14786449308620508.

[37] Henry Darcy. *Les fontaines publiques de la ville de Dijon: exposition et application...* Victor Dalmont, 1856.

[38] Maasoud Kaviany. *Principles of heat transfer in porous media*. Springer-Verlag New York, 1995. doi: 10.1007/978-1-4612-4254-3.

[39] Grigorios C Koltsakis, Andreas Konstantinou, OA Haralampous, and ZC Samaras. Measurement and intra-layer modeling of soot density and permeability in wall-flow filters. *SAE Transactions*, pages 90–102, 2006. doi: 10.4271/2006-01-0261.

[40] C Hergueta, Athanasios Tsolakis, JM Herreros, M Bogarra, Emily Price, K Simmance, APE York, and D Thompsett. Impact of bio-alcohol fuels combustion on particulate matter morphology from efficient gasoline direct injection engines. *Applied Energy*, 230:794–802, 2018. doi: 10.1016/j.apenergy.2018.08.076.

[41] M Matti Maricq and Ning Xu. The effective density and fractal dimension of soot particles from premixed flames and motor vehicle exhaust. *Journal of Aerosol Science*, 35(10):1251–1274, 2004. doi: 10.1016/j.jaerosci.2004.05.002.

[42] Jeffrey P Van Doormaal and George D Raithby. Enhancements of the simple method for predicting incompressible fluid flows. *Numerical heat transfer*, 7(2):147–163, 1984. doi: 10.1080/01495728408961817.

[43] Joel H Ferziger, Milovan Perić, and Robert L Street. *Computational methods for fluid dynamics*, volume 3. Springer, 2002. doi: 10.1007/978-3-642-56026-2.

[44] CN Davies. Definitive equations for the fluid resistance of spheres. *Proceedings of the Physical Society*, 57(4):259, 1945. doi: 10.1088/0959-5309/57/4/301.

[45] Amy Li and Goodarz Ahmadi. Computer simulation of deposition of aerosols in a turbulent channel flow with rough walls. *Aerosol Science and Technology*, 18(1):11–24, 1993. doi: 10.1080/02786829308959581.

[46] Martin Isoz and Marie Plachá. A parallel algorithm for flux-based bounded scalar redistribution. In *Proceedings of the conference Topical Problems of Fluid Mechanics*, pages 87–94. Institute of Thermomechanics of the Czech Academy of Sciences, 2022. doi: 10.14311/TPFM.2022.013.

[47] Martin Isoz. Solid phase redistribution algorithm for OpenFOAM. `https://github.com/MartinIsoz/spRedist`, 2022.

[48] Barouch Giechaskiel, Tero Lähde, Sawan Gandi, Stefan Keller, Philipp Kreutziger, and Athanasios Mamakos. Assessment of 10-nm particle number (pn) portable emissions measurement systems (pems) for future regulations. *International Journal of Environmental Research and Public Health*, 17(11):3878, 2020. doi: 10.3390/ijerph17113878.

[49] Qiang Lyu, Qisheng Ou, Weiqi Chen, Yujun Wang, Cheng Chang, Yuejin Li, Defu Che, and David YH Pui. Impacts of catalyst coating on the filtration performance of catalyzed wall-flow filters: From the viewpoint of microstructure. *Separation and Purification Technology*, 285:120417, 2022. doi: 10.1016/j.seppur.2021.120417.